

Polymeric light delivery via a C-shaped metallic aperture

Eun-Hyoung Cho,¹ Sung-Mook Kang,² J. Brian Leen,³ Sung-Dong Suh,⁴ Jin-Seung Sohn,¹ Chang-Youl Moon,¹ No-Cheol Park,^{2,*} Lambertus Hesselink,³ and Young-Pil Park²

¹Nano Fabrication Group, Material and Device Center, Samsung Advanced Institute of Technology, San 14-1, Nongseo-Dong, Giheung-Gu, Yongin-City, Gyeonggi-Do 446-712, South Korea

²Center for Information Storage Device (CISD), Yonsei University, 134 Shinchon-Dong, Seodaemoon-Ku, Seoul 120-749, South Korea

³Department of Applied Physics, Stanford University, 420 via Palou Mall, Stanford, California 94305, USA

⁴Image Architecture Laboratory, Semiconductor R&D Center, Samsung Electronics, Nongseo-Dong, Giheung-Gu, Yongin-City, Gyeonggi-Do 446-711, South Korea

*Corresponding author: pnch@yonsei.ac.kr

Received March 29, 2010; accepted April 27, 2010;
posted May 4, 2010 (Doc. ID 126186); published June 7, 2010

A polymeric light delivery system with a C-shaped metallic nanoaperture is proposed for the heat-assisted magnetic recording. This light delivery system has high optical efficiency and easy fabricability in the low temperature process that is compatible with the conventional magnetic head. The light delivery characteristics are demonstrated analytically and experimentally. In particular, the near-field spot size of the light delivery system was measured using the virtual scanning near-field optical microscopy (VSNOM) method, in which the probe tip geometry is not reflected. The probable spot size of the developed light delivery is under 100 nm at a wavelength of 780 nm from a polymeric light delivery with the C-shaped metallic nanoaperture. © 2010 Optical Society of America

OCIS codes: 050.1220, 130.5460, 180.4243, 210.0210.

1. INTRODUCTION

Near-field optical technologies, which use evanescent waves to achieve high spatial resolutions beyond the diffraction limit, have a great potential for ultrahigh density data storage. Near-field optics has been applied to various fields including biology and chemistry [1–3], electronics and photonics [4,5], nanolithography, high density optical data storage [6], and atom manipulation. Recently, an attempt has been made to realize heat-assisted magnetic recording (HAMR) using near-field optics [7]. HAMR may potentially provide a way to increase the recording density of magnetic storage by taking advantage of the heat dependence of the coercive field [8]. At elevated temperatures, the coercive field is lower, allowing data to be recorded at lower magnetic field strengths; in contrast, at room temperature, there is an increase in data stability [9].

HAMR requires a small spot size under the diffraction limit with suitable optical power to sufficiently heat the recording medium, and this poses a significant challenge. In the field of near-field optics, several methods have been proposed to achieve these specifications. Some unconventional apertures exhibit extraordinary field enhancement as well as high spatial resolutions beyond the diffraction limit, such as the C-shaped aperture of Shi *et al.* [10] and the Au nanoparticle array-based ridge waveguide of Kang *et al.* [11], Sendur and Challener's bow-tie slot antenna [12], and Tanaka and Tanaka's I-shaped aperture [13] and triangular aperture [14]. In particular, theoretical calculations and microwave experiment of Shi *et al.* [10] re-

vealed that a C-shaped aperture could increase the power throughput by a factor of 1000 compared to a conventional square aperture. Another issue in HAMR is the development of a manufacturable method of integrating a small optical delivery system, producing a sub-wavelength heating spot, with the magnetic poles in the head. High numerical aperture solid immersion lenses have been primarily used in the past, but these lenses limit the geometrical head design because they take up significant space [15]. For these reasons, the light delivery system should offer not only a field enhanced near-field spot in the exit but also be made easily and compactly while maintaining compatibility with the conventional magnetic head.

In this paper, we present what we believe to be a novel design of the beam path in the HAMR head. We fabricated the polymer waveguide, which was designed using the beam propagation method and the metallic C-shaped aperture, which was designed using the finite-difference time-domain (FDTD) method on the waveguide end facet via the focused ion beam (FIB) method. The light delivery component can be fabricated in the same batch process as the conventional magnetic head. Finally, the guiding mode and near-field characteristics in the end facet of the system are experimentally examined using near-field scanning optical microscopy (NSOM).

2. PROPOSED BEAM PATH IN THE HAMR HEAD

The proposed HAMR head is composed of a conventional magnetic recording head combined in close proximity

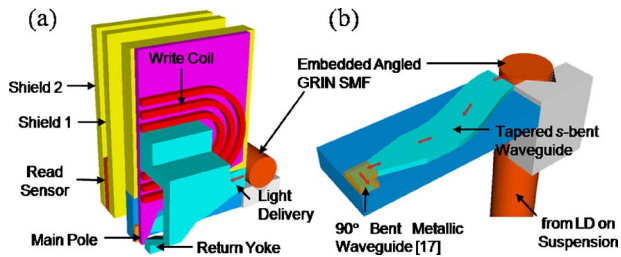


Fig. 1. (Color online) The proposed HAMR head structure: (a) HAMR head; (b) light delivery.

with a light delivery system for heating the magnetic recording medium as shown in Fig. 1. The magnetic recording head includes a coil for generating a magnetic field for recording, a recording pole for applying the magnetic field to the magnetic recording medium, and a return yoke magnetically connected to the recording pole to form a magnetic path. Regarding the waveguide location, we have chosen the recess region below the main pole. By selecting this region, we can put the waveguide end facet as close as the main pole as possible. The light delivery system includes an optical waveguide, which delivers light emitted from the light source at a distant location from the head, an optical fiber connecting the light source to the optical waveguide, and a metallic nanoaperture for enhancing the electric field from the optical waveguide. One of the most important conditions for the field enhancement is the polarization of the incoming beam. Since the polarization state is largely dependent on the geometry of the waveguide structure, a channel waveguide with a rectangular core shape has been chosen.

Figure 1(b) shows the schematic of the light delivery system in more detail. The light source is usually a semiconductor laser diode and can be located on the suspension to prevent undesirable heating of the magnetic head by the laser diode. The laser diode can be connected to the optical waveguide by conventional fiber coupling. The single mode fiber (SMF) is easily embedded in the suspension arm, as is the wire, so that the positioning of the laser diode on the *E*-block or the suspension arm mentioned above frees us from the bulky free space optics used in the structure by Challener *et al.* [16]. In the Challener structure, the bulky optics collimates the incident beam and then launches the incoming light into the waveguide through the grating coupler. Since this design has an angular tolerance of only $\pm 0.15^\circ$, the quality of the incident collimated beam is quite important. Our waveguide is

made of a polymer that can be fabricated at low temperature and it is tapered at its end to decrease the coupling loss with the SMF or a field enhanced optical element. But the symmetric tapered segment can be geometrically contacted to the media. To avoid this problem the *s*-bent waveguide is adopted. As shown in Fig. 1(b), in order to send the propagated light from the waveguide to the medium a 90° bent structure must be introduced [17,18]. In this study the tapered *s*-bent waveguide that is connected to the laser diode by the SMF is fabricated without the 90° bent metallic waveguide, allowing the near-field spot to be delivered on the recording medium. In order to accommodate a small spot size beyond the diffraction limit, the metallic nanoaperture is directly fabricated on the end facet of the waveguide, instead.

3. TAPERED *s*-BEND POLYMER WAVEGUIDE FABRICATION

The criterion for selecting the waveguide material is process compatibility with the fabrication process of the magnetic head. One of the most important factors to be considered is the process temperature. Since polymer waveguides can be fabricated at low temperature with simple steps, it was selected as the best candidate material. The mode confinement, coupling efficiency, and fabrication issues should be considered when designing the polymer waveguide. In order to satisfy these conditions, we may need to further reduce the physical dimensions of the waveguide. The coupling between the fiber and the waveguide can be quite difficult because of the mode mismatch and the effective index difference. So, it is important that the waveguide be designed with as small a refractive index difference as possible. A simulation is performed to meet the single mode operation condition at a wavelength of 780 nm with the assumption that the refractive index of the cladding is 1.410 and the cross-sectional area is $4.5 \mu\text{m} \times 1.8 \mu\text{m}$. As the index difference decreases, the required cross-sectional area for maintaining the single mode condition increases. The controllable minimum index difference in our polymer waveguide fabrication is 0.001, so we picked two index differences of 0.004 and 0.005. Fixing these index differences, we varied the width of the waveguide. As shown in Fig. 2(b), the second mode appears above the width of $6.9 \mu\text{m}$ when the index difference is 0.005 with a tolerance of around $2.5 \mu\text{m}$. Based on this result, we selected an index difference of 0.0045.

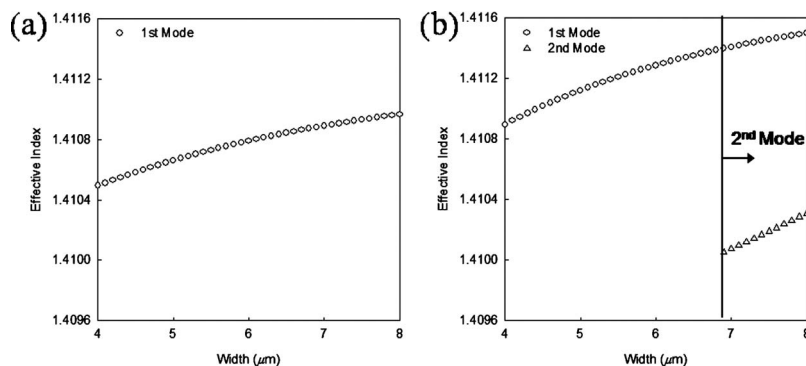


Fig. 2. Guided modes with varying width: (a) $\Delta n=0.004$ and (b) $\Delta n=0.005$.

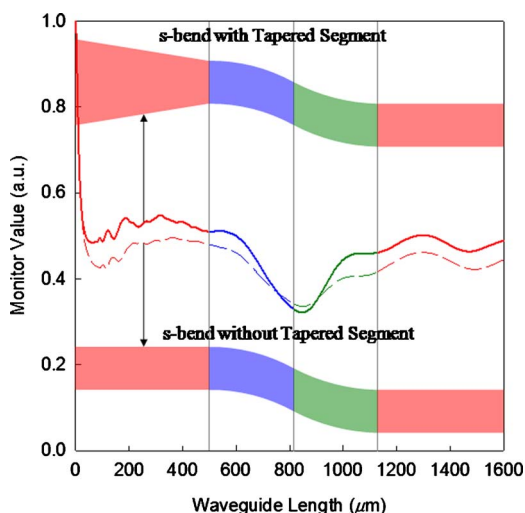


Fig. 3. (Color online) Coupling efficiency of the *s*-bend waveguide with and without the tapered segment.

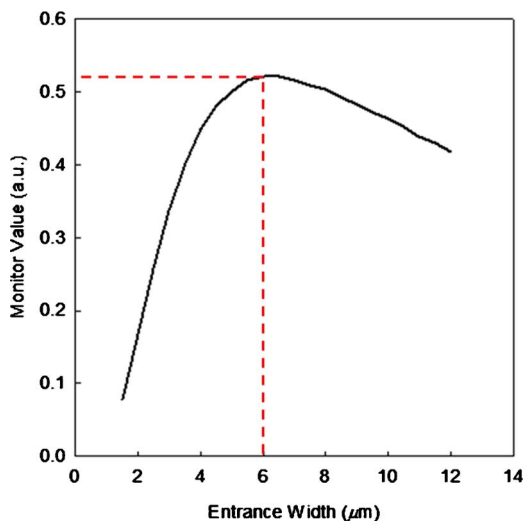


Fig. 4. (Color online) Coupling efficiency as a function of the entrance width of the waveguide.

We use an *s*-bend structure in the light delivery system to avoid the contact problem onto the medium caused by adopting a tapered segment to decrease the coupling loss as mentioned above. The loss due to the bend is largely dependent on the radius of curvature [19]. The *s*-bend structure consists of two straight waveguides and two bent segments as shown in Fig. 3. The two arcs in the *s*-bend geometry have equal radii of curvature. Considering the geometry of the main pole in the magnetic head, we can set the transverse separation at 11 μm . We found that if the radius of curvature was larger than 6000 μm , the calculated bending loss was extremely low. In order to minimize loss, we chose the following *s*-bend waveguide parameters: a 9000 μm radius of curvature, a 314.16 μm bend length, and a 2° bend angle. With these design parameters, the coupling efficiency of the *s*-bend waveguide is approximately 40%– 45% as shown in Fig. 3.

In order to increase the coupling efficiency between the polymer waveguide and the SMF or field enhanced optical element, a tapered segment structure may be used in the entrance or the exit of the polymer waveguide. In this paper we consider a tapered segment in the entrance of the waveguide without geometrical interference onto the medium by using the above *s*-bend segment. The diameter of the optical fiber core is on the order of single micrometers, and the optical spot size is approximately the same as the core diameter. The coupling efficiency can be maximized by adjusting the size of the polymer waveguide incoming end to match the beam spot size of the optical fiber. As shown in Fig. 4, we obtain an optimum entrance width of 6 μm by calculating the coupling efficiency while varying the entrance width of the waveguide. When the tapered segment is applied to the incoming end of the waveguide, the coupling efficiency can be increased to approximately 10% as shown in Fig. 3.

In comparison to conventional silica waveguides, which require high temperature processes, polymer waveguides can be easily fabricated. Since polymer waveguides can be manufactured under low temperatures, the process presented in Fig. 5 is compatible with the conventional magnetic head fabrication process. Prior to the fabrication of the polymer waveguide, refractive index tuning of the polymer material is performed to replicate the simulated index difference of 0.0045 between the core and cladding

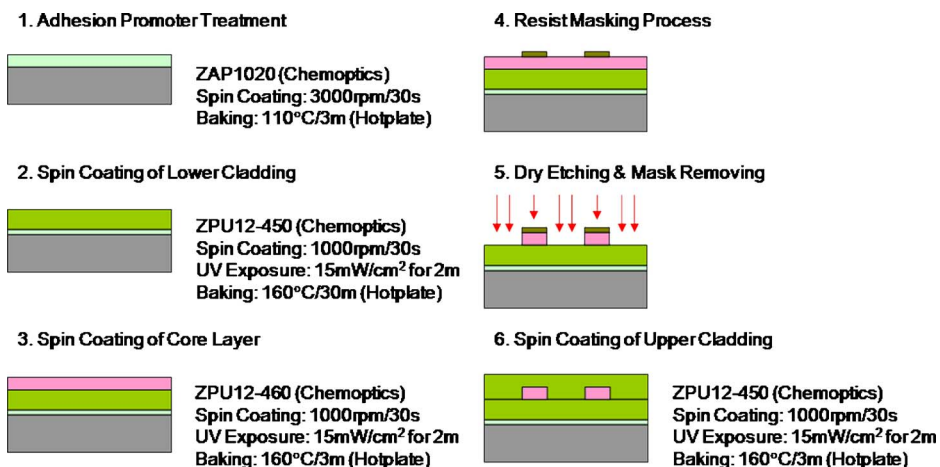


Fig. 5. (Color online) The fabrication process of the polymeric channel waveguide.

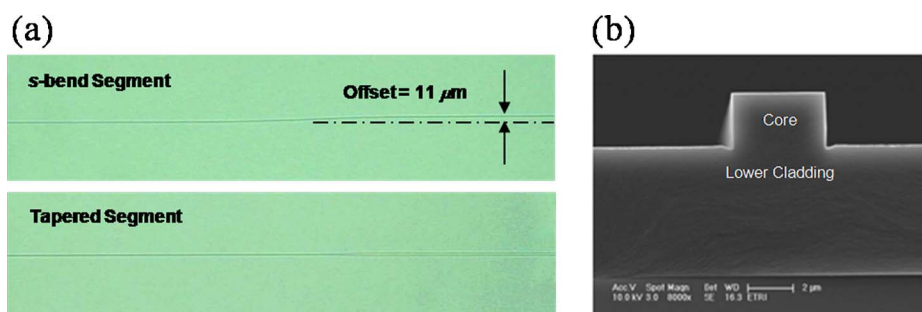


Fig. 6. (Color online) (a) Top and (b) cross-sectional views of the fabricated polymer waveguide without the upper cladding layer.

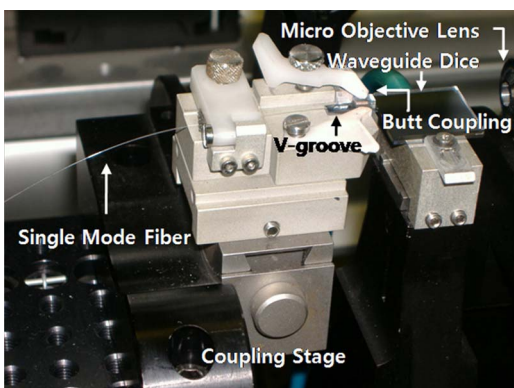


Fig. 7. (Color online) Experimental setup for polymer waveguide characterization.

layer. The refractive index difference can be estimated using a prism coupler (PCA2000, Sairon Technology, Inc.). The measured refractive index of the core is 1.4555, and that of the cladding layer is 1.4509. Note that the index difference, 0.0046, is similar to the calculated value. The main fabrication process of the polymer waveguide starts with spin coating the lower cladding material onto a substrate after the adhesion treatment. Next, the lower cladding layer is coated and cured with 15 mW cm^{-2} ultraviolet exposure for 2 min. Similarly, the core material is coated and cured. A waveguide pattern is formed using conventional photolithography and dry-etching. Finally, the waveguide is finished by adding the upper cladding layer. Figure 6 shows the top view of the tapered *s*-bend waveguide and the side view of the core and low cladding of the waveguide before the upper cladding layer process. The core layer is shown in the top view because there is a refractive index difference between the core and cladding layer.

In order to decide whether the guided mode in the fabricated polymer waveguide is single, an experimental setup is arranged as shown in Fig. 7. The SMF is butt-coupled to the waveguide using the V-shaped groove, and

a 780 nm pigtailed wavelength source is applied. As shown in Fig. 8, the light in the waveguide is guided, which maintains the much stronger guiding mode. The peak scanning result of the guiding mode ensures that the waveguide has a single mode and no second mode. Moreover, a bright output spot in the end of the channel waveguide is observed. The bending loss of the *s*-bend polymer waveguide is estimated at 780 nm wavelength. As shown in Fig. 9, the bending loss decreases with the increase in the radius of curvature. In the case of a refractive index difference of 0.0046, the fabricated waveguide has an extremely small bending loss of less than 5 dB. It is noted that the developed *s*-bend waveguide has excellent waveguide characteristics and can be easily fabricated in low temperatures while maintaining process compatibility with the conventional magnetic head.

4. C-SHAPED METALLIC WAVEGUIDE FABRICATION

Since the spot size of the *s*-bend polymer waveguide is very large, the waveguide cannot be directly applied to the magnetic head, which requires a small spot size under the diffractive limit. As mentioned above, we first tried to make the nanoaperture on the end face of the fabricated polymer waveguide. We analyzed the relation between the resonant frequency and the metal layer thickness using the numerical FDTD method (commercial code “XFDTD 6.3” from Remcom [20]) before performing the fabrication. In order to treat real metals accurately, the modified Debye model [21] was used to compute the complex permittivity for Au. Using the experimental refractive index data for Au [22] at a wavelength of 780 nm, the parameters of the modified Debye model are determined to be $\epsilon_s = -470$, $\epsilon_\infty = 1.001$, $\tau = 2.1 \times 10^{-15} \text{ s}$, and $\sigma = 1.986 \times 10^6 \text{ S m}^{-1}$, where ϵ_s is the static permittivity, ϵ_∞ is the permittivity at the infinite frequency which should not be less than 1, σ is the conductivity, and τ is the relaxation time. The total height of the aperture is 270 nm and the total width of the aperture is 180 nm. The aperture has a

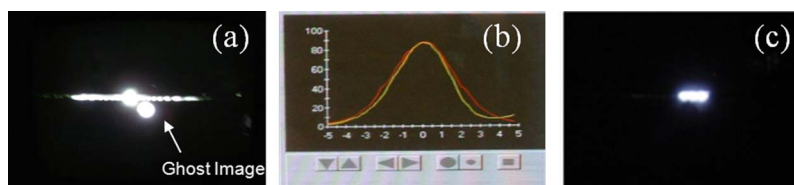


Fig. 8. (Color online) The (a) guiding mode image, (b) peak scanning image, and (c) output spot image of the polymer waveguide.

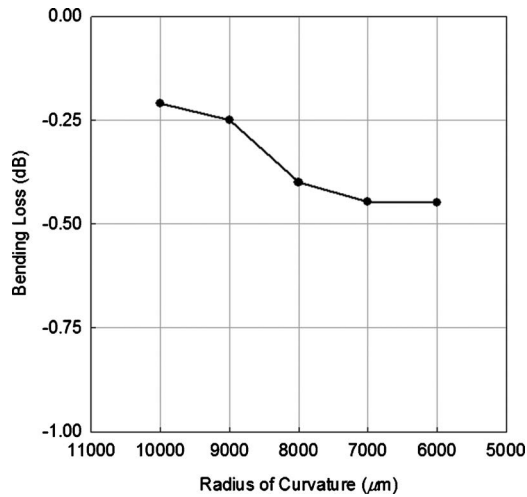


Fig. 9. Measured bending loss of the polymer waveguide.

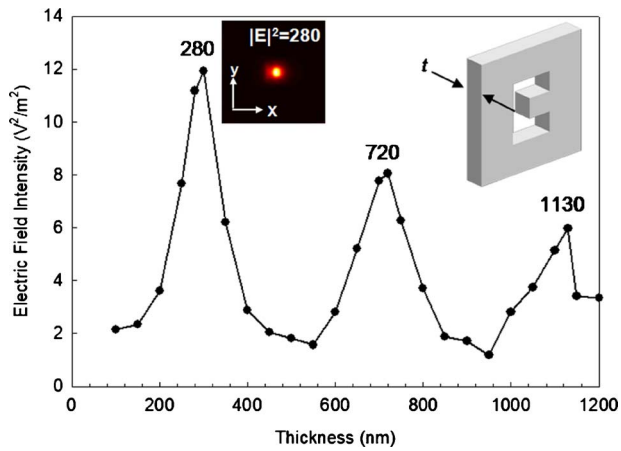


Fig. 10. (Color online) Change in electric field intensity with respect to the metal layer thickness.

central waist of 90 nm and a ridge height of 70 nm. The spot size can be controlled by changing the central waist and the ridge height. Through the FDTD simulation, we found gradual generation of more highly resonant transmission modes and that the $|E|^2$ intensity is decreased as the thickness of the metal layer increases as shown in Fig. 10. Note that at resonant thickness the field enhancement characteristics are maintained despite the large thickness. The calculated full width at half-maximum (FWHM) spot sizes are 91 nm in the x -direction and 96 nm in the y -direction at a distance of 20 nm after passing through the nanoaperture. Since the C-shaped nanoaperture of 280 nm thickness has a maximum $|E|^2$ intensity, we chose this thickness of 280 nm for the fabrication.

We fabricated a C-shaped metallic nanoaperture on the polymer waveguide using the FIB method. An Au layer of 280 nm is deposited on the output surface of the waveguide. Since it is difficult to fabricate the nanoaperture in the middle of the core layer of the waveguide, we first applied an O₂ plasma reactive ion etching process to the output surface of the waveguide. The core and cladding layers have different refractive indices and etching properties. Using this process, the core layer can be made to protrude relative to the cladding layer. In this way, we can easily find the core layer and fabricate the nanoaperture in the middle of the core layer by FIB milling (FEI Strata 235DB dual-beam machine). The FIB milling conditions that minimize the fabrication error are as follows: a dwell time of 1 μs, an ion beam current of 2 pA, an ion column aperture of 1 pA, an overlap of 50%, and a dose time of 6 s. The fabricated C-shaped nanoaperture on the polymer waveguide is shown in Fig. 11.

5. NEAR-FIELD CHARACTERISTICS EVALUATION

It is important to experimentally characterize the apertures in order to verify that they perform as expected. This is done both in the far- and near-fields. In the near-field, the goal is to obtain an image of the near-field distribution of the aperture using a near-field probe. However, because the C-shaped nanoaperture produces such a small spot, it is very difficult to create a near-field transmission probe that will accurately sample the field of interest. The standard near-field scanning optical microscope transmission probe has a circular aperture that is 50–100 nm in diameter and a commensurate resolution in this range. The size of the field from the C-shaped aperture is on the order of this size range and, therefore, the resultant image is a convolution of the two fields. Furthermore, because the collection is performed in the near-field, the resulting image is a complex convolution of the electric and magnetic fields of one aperture and those of the other. For this reason, it is impossible to perform a standard deconvolution and we need to turn to more complex data analysis methods in order to interpret the results of the C-shaped nanoaperture NSOM images. The method we have chosen has been termed the virtual scanning near-field optical microscopy (SNOM) or VSOM [23]. This method allows us to simulate the expected NSOM image based on the C-shaped nanoaperture and the NSOM probe aperture used in the scan. By comparing this result with the experimental data and assuming that the circular aperture of the NSOM probe is well modeled with FDTD techniques, we can obtain an estimate of the spot size of the C-shaped aperture using simple scaling.

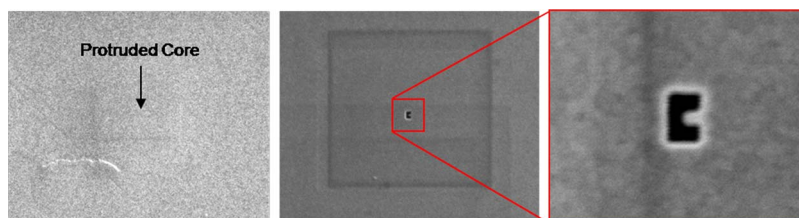


Fig. 11. (Color online) Fabricated C-shaped nanoaperture on a polymer waveguide.

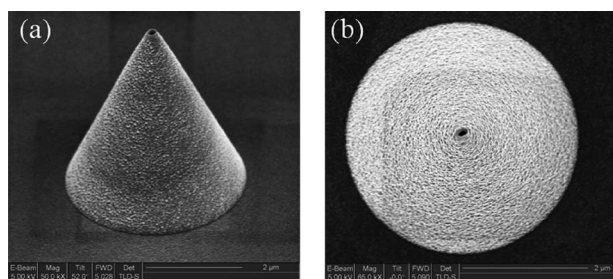


Fig. 12. FIB milled probe tip: (a) tilted and (b) top views.

Using the Lorentz reciprocity theorem [24], one can relate these fields and derive an expression for the detected electric field as a function of the interaction between the reciprocal and experimental fields. It is then possible to simulate both the tip and sample separately and directly calculate the detected quantity. The advantages of this method are that the two simulations are done independently and that simulation at every point in the scan is not necessary [25,26]. It is also possible to displace the reciprocal and experimental fields with respect to each other and calculate the signal generated at any other point. Using this formalism, one can use FDTD simulations of both the tip and of the sample to calculate the final image.

For the power budget, we consider that the power of around 1 mW is available on the HAMR medium which can be heated up to 235°C and can be easily recorded by the magnetic head [27]. The coupling efficiency between the embedded angled gradient index (GRIN) SMF and the polymer waveguide is approximately 30%. The propagation efficiency of the polymer waveguide with the 90° bent metallic waveguide is around 10%, and the transmission efficiency of the aperture is calculated by about 50%. Therefore, the total efficiency of the light delivery is 1.5%. Considering this power budget the required power of the laser source will be over 67 mW. Since the conventional distance between the magnetic head and the medium is under 10 nm, the design and the measurement for the nanoaperture for the HAMR have to be performed at the mentioned distance.

The real probe tip has the ellipsoidal probe aperture which is created by the FIB milling process as shown in Fig. 12. To calculate the VSNO image, the real probe tip is chosen with an asymmetric ellipsoidal aperture of

width 144 nm × 77 nm. As mentioned above, the C-shaped aperture has a FWHM spot size of 96 nm × 91 nm. Considering a probe tip with a 40 nm distance between the probe tip and the C-shaped aperture, the VSNO image can be obtained as shown in Fig. 13. Figure 13(a) shows the VSNO image with the probe aperture horizontally oriented with respect to the central waist of the C-shaped aperture. The FWHM spot size is 891 nm × 293 nm and is much larger than the case in which we consider only the electric field intensity. When the probe aperture is vertically oriented with respect to the C-shaped aperture, the FWHM spot size is so large as 450 nm × 240 nm. Nevertheless, this size is still smaller than that of the horizontal orientation. Note that the orientation and the shape of the probe tip have an effect on the FWHM spot size of the C-shaped aperture. Therefore, we have to perform angular alignment between the tip and the sample to minimize the spot size.

To characterize the near-field spot size of the C-shaped aperture on the polymer waveguide module as shown in Fig. 14(a), the NSOM experimental system is set up as shown in Fig. 14(b). By adjusting the polarization controller in the system, we can maximize the near-field scattering image. Figures 15(a) and 15(b) show the minimum and the maximum scattering images, respectively. After maximizing the near-field scattering image, the probe tip approaches the waveguide module, and the NSOM image is obtained by finely scanning the probe tip in the near-field region. Since we cannot know whether the orientation of the sample matches well with the aperture, the NSOM test is performed while changing the orientation of the probe tip. Figure 16 shows the NSOM images with different orientations of the C-shaped aperture. In the case of a 45° orientation, the NSOM spot size is 375 nm × 133 nm, which is the smallest value in our test. As mentioned above, in the 45° sample orientation the probe tip is vertically oriented to the central waist of the C-shaped aperture. The behavior of the measured spots matches quite well with the theoretical expectations from the VSNO method. Specifically, the spot is elongated with roughly the same ratio and the spot size increases substantially when the probe tip is rotated with respect to the C-shaped aperture. Moreover, the observed spot size is not the real spot size from the aperture. The NSOM signal information includes the asymmetrical geometry of the probe tip as well as the real spot size from the aper-

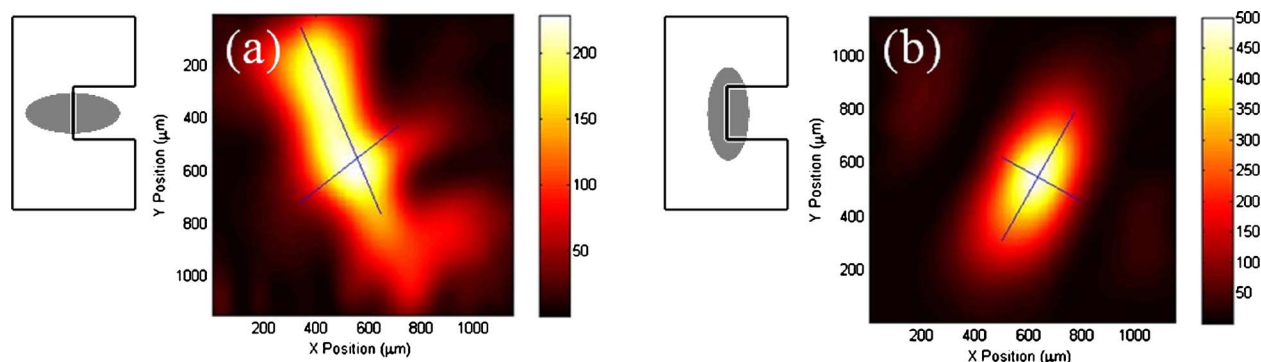


Fig. 13. (Color online) Calculated spot image using the VSNO method oriented (a) horizontally and (b) vertically with respect to the central waist of the C-shaped aperture.

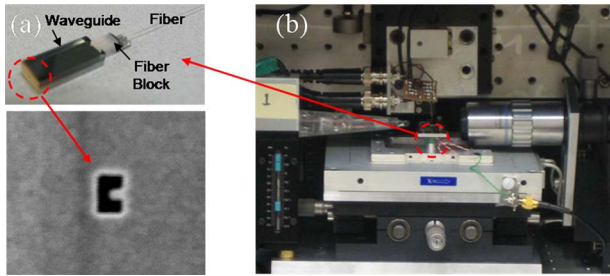


Fig. 14. (Color online) (a) The waveguide module with the C-shaped aperture and (b) the experimental setup for the NSOM test.

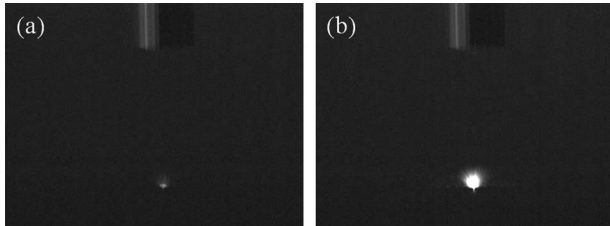


Fig. 15. Near-field scattering images from the C-shaped aperture on the polymer waveguide: (a) mismatched and (b) matched polarizations.

ture as mentioned in the VSOM simulation. We need to detangle the real spot size of the C-shaped aperture from this measured spot size. By using the calculated spot sizes in the above VSOM simulation and scaling the simulated spot size of the C-shaped aperture by the ratio of the measured and VSOM spot sizes, including the geometry of the probe tip, the expected spot size is found to be about 100 nm at a wavelength of 780 nm. The discrepancy in the probable spot size may be due to a different separation (i.e., scanning height) between the probe and the C-shaped aperture. A VSOM simulation at a distance of 10 or 20 nm may show spot sizes that more closely match the expected value.

6. CONCLUSIONS

The polymeric light delivery with a C-shaped metallic aperture was developed in the low temperature process, maintaining process compatibility with the conventional magnetic head. The polymer waveguide has an s-bend and tapered structure to allow easy application to the

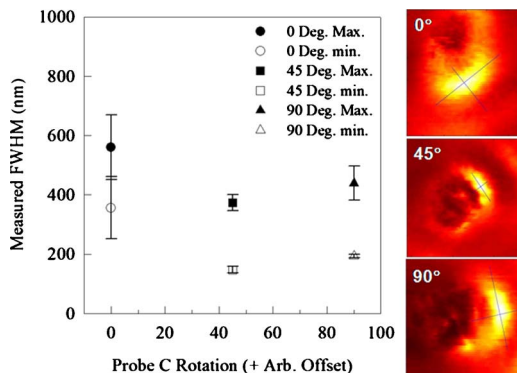


Fig. 16. (Color online) NSOM images at various angles of probe tip and C-shaped aperture.

head and to increase the coupling efficiency with the single mode fiber (SMF). The characteristics of the waveguide were estimated analytically and experimentally.

In order to obtain the small spot size that permits high density recording in HAMR, the C-shaped metallic aperture was fabricated on the output surface of the waveguide using the FIB method. To characterize the near-field performance of the fabricated light delivery, NSOM was performed. The measured NSOM spot size has a remarkable dependence on the orientation and the geometry of the probe tip. To separate the real spot size from the NSOM image, the VSOM method was applied. The probable spot size of the developed light delivery is under 100 nm at a wavelength of 780 nm from a polymeric light delivery with the C-shaped metallic nanoaperture. The proposed polymeric light delivery is a promising candidate for HAMR.

ACKNOWLEDGMENT

This work was supported by the National Research Foundation of Korea (NRF) grant funded by the Korean government (No. 2009-0086278).

REFERENCES

1. A. Harootunian, E. Betzig, M. Isaacson, and A. Lewis, "Super-resolution fluorescence near-field scanning optical microscopy," *Appl. Phys. Lett.* **49**, 674–676 (1986).
2. D. P. Tsai, A. Othonos, M. Moskovits, and D. Uttamchandani, "Raman spectroscopy using a fiber optic probe with subwavelength aperture," *Appl. Phys. Lett.* **64**, 1768–1770 (1994).
3. N. Van Hulst, J.-A. Veerman, M. Garcia-Parajo, and L. Kuipers, "Analysis of individual (macro)molecules and proteins using near-field optics," *J. Chem. Phys.* **112**, 7799–7810 (2000).
4. E. Betzig, A. Harootunian, A. Lewis, and M. Isaacson, "Near-field diffraction by a slit: implications for superresolution microscopy," *Appl. Opt.* **25**, 1890–1900 (1986).
5. J. Hsu, "Near-field scanning optical microscopy studies of electronic and photonic materials and devices," *Mater. Sci. Eng. R.* **33**, 1–50 (2001).
6. A. Partovi, D. Peale, M. Wuttig, C. A. Murray, G. Zydzik, L. Hopkins, K. Baldwin, W. S. Hobson, J. Wynn, J. Lopata, L. Dhar, R. Chichester, and J. H.-J. Yeh, "High-power laser light source for near-field optics and its application to high-density optical data storage," *Appl. Phys. Lett.* **75**, 1515–1517 (1999).
7. W. A. Challener, T. W. McDaniel, C. D. Mihalcea, K. R. Mountfield, K. Pelhos, and I. K. Sendur, "Light delivery techniques for heat-assisted magnetic recordings," *Jpn. J. Appl. Phys., Part 1* **42**, 981–988 (2003).
8. M. Alex, A. Tselikov, T. McDaniel, N. Deeman, T. Valet, and D. Chen, "Characteristics of thermally assisted magnetic recording," *IEEE Trans. Magn.* **37**, 1244–1249 (2001).
9. P. L. Lu and S. H. Charap, "Magnetic viscosity in high-density recording," *J. Appl. Phys.* **75**, 5768–5770 (1994).
10. X. L. Shi, R. L. Thornton, and L. Hesselink, "A nano-aperture with 1000× power throughput enhancement for very small aperture laser system (VSAL)," *Proc. SPIE* **4342**, 320–326 (2002).
11. S.-M. Kang, J. Han, T. Kim, N.-C. Park, K.-S. Park, B.-K. Min, and Y.-P. Park, "Multiple excitation of localized surface plasmon to create a 10 nm × 10 nm strong optical spot using an Au nanoparticle array-based ridge waveguide," *Opt. Express* **18**, 1576–1585 (2010).
12. I. K. Sendur and W. A. Challener, "Near-field radiation of bow-tie antennas and apertures at optical frequencies," *J. Microsc.* **210**, 279–283 (2003).

13. K. Tanaka and M. Tanaka, "Simulation of an aperture in the thick metallic screen that gives high intensity and small spot size using surface plasmon polariton," *J. Microsc.* **210**, 294–300 (2003).
14. K. Tanaka, M. Oumi, T. Niwa, S. Ichihara, Y. Mitsuoka, K. Nakajima, T. Ohkubo, H. Hosaka, and K. Itao, "High spatial resolution and throughput potential of an optical head with a triangular aperture for near-field optical data storage," *Jpn. J. Appl. Phys., Part 1* **42**, 1113–1117 (2003).
15. T. Rausch, C. Mihalcea, K. Pelhos, D. Karns, K. Mountfield, Y. A. Kubota, X. W. Wu, G. P. Ju, W. A. Challener, and C. B. Peng, "Near field heat assisted magnetic recording with a planar solid immersion lens," *Jpn. J. Appl. Phys., Part 1* **45**, 1314–1320 (2006).
16. W. A. Challener, C. Peng, A. V. Itagi, D. Karns, W. Peng, Y. Peng, X. Yang, X. Zhu, N. J. Gokemeijer, Y.-T. Hsia, G. Ju, R. E. Rottmayer, M. A. Seigler, and E. C. Gage, "Heat-assisted magnetic recording by a near-field transducer with efficient optical energy transfer," *Nature Photon.* **3**, 220–224 (2009).
17. P. Hansen, B. Leen, and L. Hesselink, "Design of a sub-wavelength bent C-aperture waveguide," *Opt. Lett.* **32**, 1737–1739 (2007).
18. B. Leen, E.-H. Cho, S.-D. Suh, P. Hansen, J.-S. Sohn, S.-H. Choa, and L. Hesselink, "90° bent metallic waveguide with a tapered C-shaped aperture for use in HAMR," *Proc. SPIE* **6620**, 66200R (2007).
19. L. D. Hutcheson, I. A. White, and J. J. Burke, "Comparison of bending losses in integrated optical circuits," *Opt. Lett.* **5**, 276–278 (1980).
20. Remcom Inc., XFDTD 6.3 software.
21. K. Kunz and R. Lubbers, *The Finite Difference Time Domain Method for Electromagnetics* (CRC, 1996).
22. E. D. Palik, *Handbook of Optical Constants of Solids* (Academic, 1996).
23. J. A. Matteo, Ph.D. dissertation (Stanford University, 2004).
24. L. Landau, E. Lifchitz, and L. Pitaevskii, *Electrodynamics of Continuous Media* (Pergamon, 1984).
25. S. H. Fan, I. Appelbaum, and J. D. Joannopoulos, "Near-field scanning optical microscopy as a simultaneous probe of fields and band structure of photonic crystals: a computational study," *Appl. Phys. Lett.* **75**, 3461–3463 (1999).
26. H. Hatano and S. Kawata, "Applicability of deconvolution and nonlinear optimization for reconstructing optical images from near-field optical microscope images," *J. Microsc.* **194**, 230–234 (1999).
27. E. Komura, K. Shimazawa, K. Tanaka, and H. Hirabayashi, "Magnetic head and magnetic recording method," Japanese patent application 2005-004901 (01 06, 2005).